

# **Final Report to BSEE: Distributed Chemical Sensing for Sub-surface Oil Spill Sensing**

**Work Performed Under Contract: E14PC00016**

**Submitted by:**

**Wei-Chuan Shih, Ph.D.  
University of Houston  
4800 Calhoun Rd.  
Houston TX 77204  
(713) 743-4454  
wshih@uh.edu**

**Submitted to:**

**Bureau of Safety and Environmental Enforcement  
(BSEE)  
Oil Spill Response Research Branch**

**May 21, 2017**

## **Acknowledgements**

This study was funded by the Bureau of Safety and Environmental Enforcement (BSEE), U.S. Department of the Interior, Washington, D.C., under Contract E14PC00016.

## **Disclaimer**

This final report has been reviewed by the BSEE and approved for publication. Approval does not signify that the contents necessarily reflect the views and policies of the BSEE, nor does mention of the trade names or commercial products constitute endorsement or recommendation for use.

## **Table of Contents**

<b>Executive Summary</b>	<b>4</b>
<b>1 Introduction</b>	<b>5</b>
<b>2 Background and Significance</b>	<b>5</b>
<b>3 Research Objectives</b>	<b>5</b>
<b>4 Results and Discussion</b>	<b>5</b>
<b>5 Conclusions</b>	<b>18</b>
<b>6 Recommendations for Future Work</b>	<b>18</b>
<b>7 References</b>	<b>19</b>

## Executive Summary

In sub-surface offshore oil spills, *sensing innovation* is urgently needed to replace current pipeline monitoring, which is indirect and prone to misses and false alarms. In this project, we have investigated the capability of chemical sensing by integrating plasmonic nanostructures, multi-modal spectroscopic sensing, and optical fiber technology, with the ultimate goal toward *real-time leak quantification*. The novel sensor would perform 24/7, night & day, distributed, and automated operations. Further, since such a low-cost system requires minimal power and maintenance, it has the potential to be deployed on multiple platforms to form a cross-platform network for spill trajectory monitoring and environmental forensics.

We have developed a novel plasmonic nanostructures, nanoporous gold disks (NPGD), for multi-modal spectroscopic sensing together with optical fiber technology. NPGD possess large specific surface area due to their extensive nanoporous network. NPGD also contain numerous plasmonic hot-spots throughout the porous network. For selective molecular binding of hydrocarbons, we have developed a compatible aryl-bisthiolate functional surface. Based on surface-enhanced Raman scattering (SERS) and localized surface plasmon resonance (LSPR), we have demonstrated the detection and quantification of various polycyclic aromatic hydrocarbon species. We have developed two portable field prototype systems and tested the SERS and LSPR sensing performance at Ohmsett. The sensors were capable of detecting ppm level PAH in salt water.

Based on the proof of concept sensor performance, we believe further engineering can push the sensors to achieve ppm level detection of PAH and BTEX in the sub-sea environment. Due to the compactness and power-efficiency of these sensors, future integration with ROV and/or AUV is feasible.

## **Introduction**

In sub-surface offshore oil spills, *sensing innovation* is urgently needed to replace current pipeline monitoring, which is indirect and prone to misses and false alarms. In this project, we have investigated the capability of chemical sensing by integrating plasmonic nanostructures, multi-modal spectroscopic sensing, and optical fiber technology, with the ultimate goal toward *real-time leak quantification*. The novel sensor would perform 24/7, night & day, distributed, and automated operations. Further, since such a low-cost system requires minimal power and maintenance, it has the potential to be deployed on multiple platforms to form a cross-platform network for spill trajectory monitoring and environmental forensics.

## **Background and Significance**

Subsea sensing of crude oil spills has been of great interest in environmental protection and disaster management. However, this challenge has not been met with reliable and robust technology. Our approach addresses many challenges optical sensor faces. By the field enhancement of plasmonic nanostructures, the molecular fingerprints can be highly amplified. Existing detection limit of plasmon-enhanced sensor can be as good as single molecule level. Second, by employing multiplexing and optical fiber links, a single sensing hub can manage ~100 sensing nodes whose location can be strategically planned before deployment, thus greatly improving spatial coverage. Thirdly, together with the intrinsic molecular fingerprinting provided by optical spectroscopy, computational sensing algorithms will further enhance the detection sensitivity, selectivity, and quantification accuracy. Thus, we envision our approach to provide high sensitive, discriminative, and robust detection of trace oil leaks.

## **Research Objectives**

The plasmonic nanostructures of choice is monolithically fabricated nanoporous gold disks (NPGD) recently developed by our group [1-19]. NPGD possess large specific surface area due to their internal nanoporous network. NPGD also contain numerous plasmonic hot-spots throughout the internal volume, which has enabled the demonstration of the following sensitive surface-enhanced spectroscopies:

1. Surface-enhanced Raman spectroscopy (SERS)
2. Localized surface plasmon resonance (LSPR) extinction spectroscopy

## **Results and Discussion**

### **Summary Points of Most Significant Technical Achievement(s)**

1. SERS-based sensing for polycyclic aromatic hydrocarbon (PAH) on NPGD.
2. LSPR-based sensing for polycyclic aromatic hydrocarbon (PAH) on NPGD.
3. Test field-portable instrument prototype at Ohmsett

### **Identify and investigate key parameters in fabricating NPGD arrays**

Experiments have shown the performance of NPGD substrate is strongly influenced by structural design such as disk diameter and thickness, under-layer thickness and patterning depth. In order for such highly effective SERS substrate to be routinely fabricated and to further enhance its performance, it is important to determine the correlation between the SERS activity and these fabrication parameters. To this end, we have investigated these parameters and developed a

design guideline. For example, **Figure 1** shows the tunable LSPR peak by varying the diameter of disks.

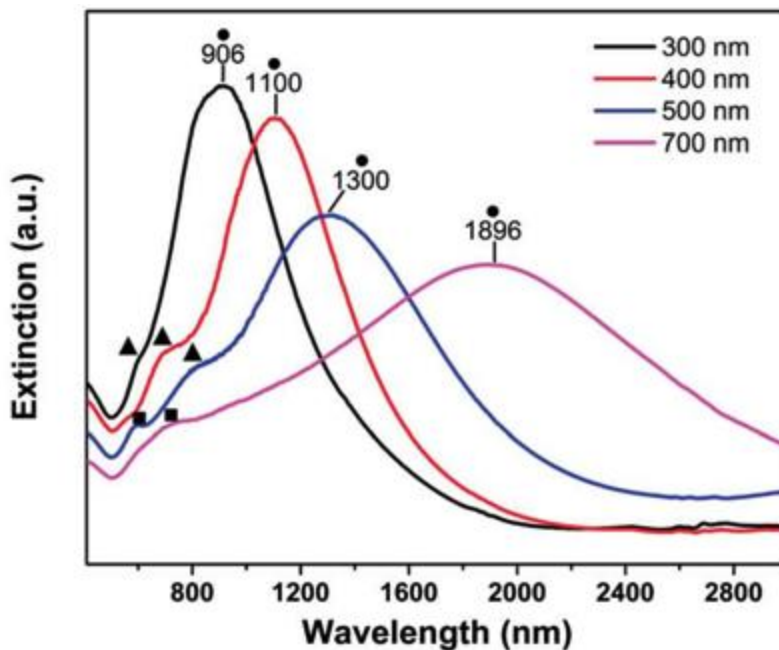


**Figure 1.** Tunable LSPR by varying disk diameter.

### SERS-based sensing for polycyclic aromatic hydrocarbon (PAH) on NPGD arrays

We have focused on the use of nanotechnology coupled with surface-enhanced Raman scattering (SERS) as means for detecting PAH molecules. Our efforts have thus focused on fabricating thin film modified porous material as well as evaluating its performance in detecting PAH molecules, as shown in **Figure 2**. Our steps on this work were aimed at the molecular design and the synthesis of the bithiolated aromatic molecule, hexyl-functionalized aryl-bisthiol ( $\text{H}(\text{CH}_2)_6\text{OC}_6\text{H}_3(\text{CH}_2\text{SH})_2$ ) (C6ArDT), to serve as seeds for the self assembled monolayer (SAM) modification on the targeted substrate. C6ArDT offers unique characteristics, such that: I) it improves the thermal stability and the life time of the thin film via the chelating effect of two headgroups per molecule to the gold surface, II) improve the interaction between the SAM and PAH molecules via  $\pi$ - $\pi$  interaction, and III) SAMs formed from such bithiolated molecules are inherently expected to have a lower packing density compared to other SAM systems that have been used in comparable studies. The latter feature allows for a facile way for generating SAMs functionalized substrates with high reproducibility in their sensing capability.

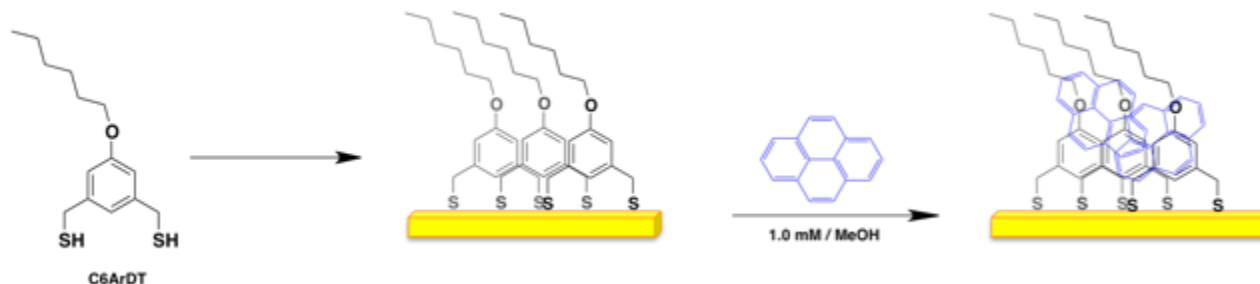


**Figure 2.** Illustration of C6ArDT SAMs formed on NPGD for trapping pyrene molecules.

## Organic thin film characterization on NPGDs Substrates

Following the optimization of the NPGDs substrate fabrication to give the highest SERS intensity, organic thin films of the newly synthesized bithiolate molecule (C6ArDT) were generated by solution deposition of the porous disk substrates in ethanol or THF solutions of C6ArDT for 48 hours. In addition, SAMs of *n*-dodecanethiol (DDT) were also formed using the same concentration and incubation time to serve as a reference for this study. X-ray photoelectron spectroscopy (XPS) analysis of the generated thin films allows for examining the chemical nature of the thiolated head group and the composition of the respected organic film. **Figure 3** shows the XPS spectra for the regions associated with Au4f, S2p, O1s, and C1s core electrons generated from these SAMs. Analysis of the S2p region of all the films confirms film formation as indicated by the presence of peaks at ~162 eV and 163.4 eV S2p<sub>3/2</sub> and S2p<sub>1/2</sub> respectively. For this region, S2p peaks at ~162 eV and 163.4 eV S2p<sub>3/2</sub> are indicative of sulfur atoms bound on gold. Furthermore, All S2p region of all SAMs, except those of DDT, show also peaks at 163.2–134.4 eV indicating the presence of unbound thiol. In fact, initial assessment of the S2p XPS spectra of C6ArDT SAMs generated from ethanolic solution shows that films from this system portray a high level of unbound thiol (54%). Thus, in order to improve the binding percentage of the bithiolated headgroups, C6ArDT solutions of THF were tested at concentration of 1mM, 0.1 mM, and 0.01mM, see **Figure 3** and **Table 1**.

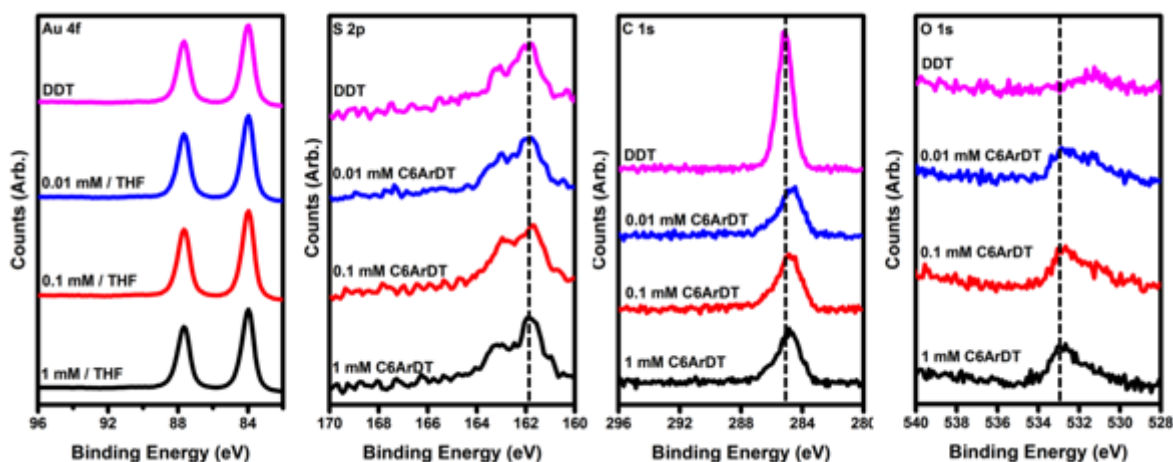


**Figure 3.** XPS spectra of Au4f, C1s, O1s, and S2p core electron emitted from SAMs of DDT and C6ArDT of different solution concentrations in THF (1.0 mM, 0.10 mM, 0.010 mM).

**Table 1.** Ratios of the S 2p, Au 4f XPS Peak Area for the C6ArDT SAMs and Those of C12, as well as Their Relative Packing Densities <sup>a</sup>

SAM (mM)	%Bound Thiol	(S 2p / Au 4f)	Relative Packing Density
C12 (1.0)	100 %	0.0087	1.00
C6ArDT (1.0)	82 %	0.0053	0.61
C6ArDT (0.10)	88 %	0.0049	0.56
C6ArDT (0.010)	94 %	0.0041	0.46

<sup>a</sup> All the S 2p / Au 4f ratios of the bithiolated monolayers (C6ArDT) are multiplied by a factor of 0.5 to allow for a fair comparison with monothiolated monolayers (C12).

Following XPS analysis of the C6ArDT monolayer formed from different concentration, we characterized these monolayers using SERS. All monolayers used herein are adsorbed on NPGDs substrates that are covered by 4 nm thick outer gold layer. **Figure 4** shows SERS spectra of the C6ArDT. Featured peaks include 668, 699, 993, 1217, 1297, 1332, and 1590  $\text{cm}^{-1}$ . Based on earlier Raman analysis of benzylthiol derivatives, the observed peaks correspond to C–S stretching (668  $\text{cm}^{-1}$ ), benzene ring breathing (993  $\text{cm}^{-1}$ ) and C–C ring stretching (1590  $\text{cm}^{-1}$ ) [Phys.Chem.Chem.Phys.2015,17,7095]. As for bands at 1217  $\text{cm}^{-1}$ , such band may correspond to benzylic  $\text{CH}_2$  twisting mods.

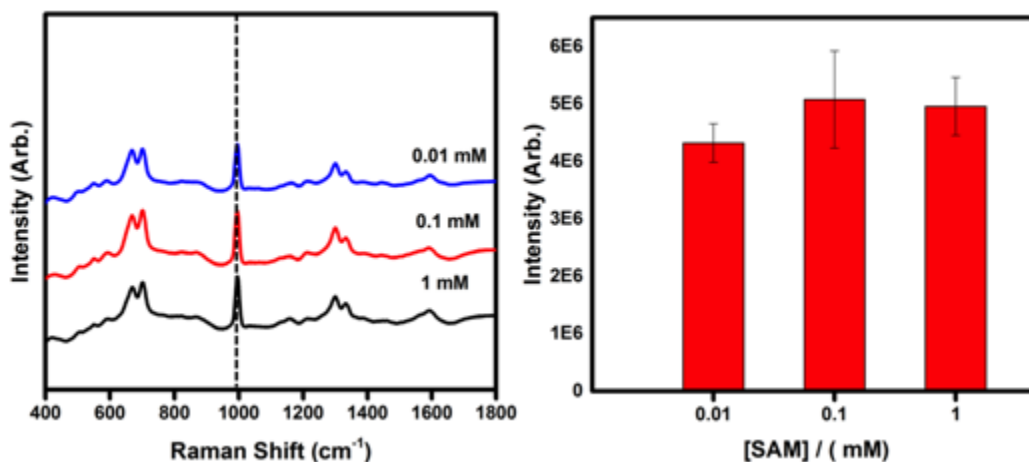


**Figure 4.** SERS spectra of C6ArDT SAMs generated from 1, 0.1, 0.01 mM THF solution on NPGD.

The SERS spectra of the C6ArDT SAMs in **Figure 4** also show that the peak intensities for all bands of the SAMs formed from 0.01 mM concentration are lower than bands in the other two SAMs. In addition, the bands' intensities in later two types of films are incrementally identical. These results corroborate with the relative packing densities obtained by the XPS analysis, thus further supporting the notion that lowering the concentration of the bithiolated molecule not only improved the percent binding of the headgroups but also provide a monolayer with lower density of molecules, an issue of vital importance in designing SAMs to serve as adhesion layers for detecting PAH molecules.

### SERS Detection of PAH molecules

Prior to evaluate the SERS detection of PAH molecules (pyrene [PY], anthracene [ANT], and benzo[a]pyrene [BaP]) on the newly designed NPGDs platform, we collected and analyzed Raman spectra of these PAH molecules in solid state (**Figure 5**). Based on assignment in the literature, Raman peaks for PY are 407  $\text{cm}^{-1}$  skeletal stretching mode, 594  $\text{cm}^{-1}$  CC breathing mode, 1246  $\text{cm}^{-1}$  CC stretching and CH in plane bending mode, and 1406  $\text{cm}^{-1}$  CC stretching and ring stretching mode. As for ANT molecules; the observed strong peaks are 395  $\text{cm}^{-1}$  CC breathing mode, 750  $\text{cm}^{-1}$  CC ring stretching (12 C) mode, and 1404  $\text{cm}^{-1}$  CC ring stretching (14 C) mode [Anal. Chem. 2011, 83, 2518]. As for BaP, The main Raman peaks are those at 1250  $\text{cm}^{-1}$ , 1380  $\text{cm}^{-1}$ , and 1650  $\text{cm}^{-1}$ , which correspond to C–H bending, C–H in plan bending and ring deformation, as well as C–C associated with ring stretching mode.

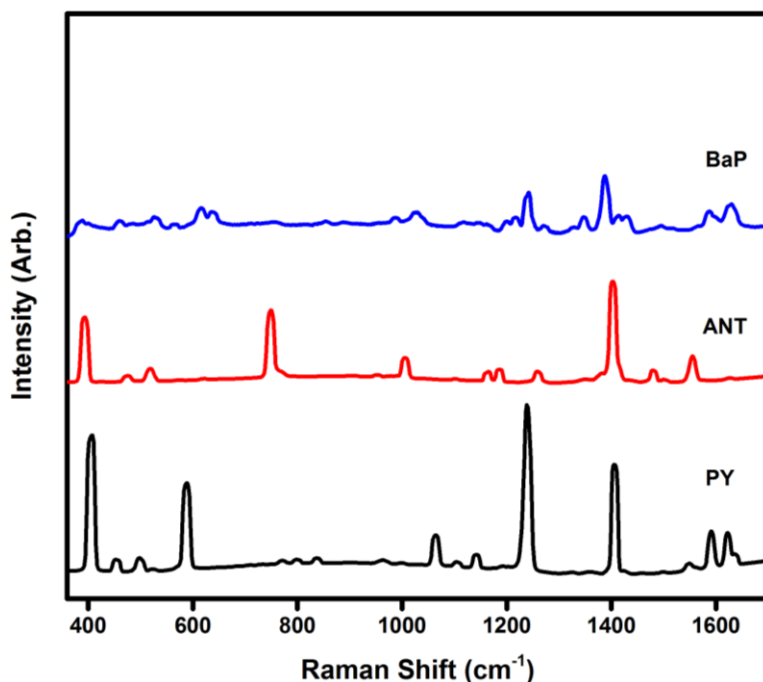


**Figure 5.** Raman spectra of solid PY (black) ANT (red), and BaP (blue).

### **Limit of Detection (LOD) of PAH Molecules**

Following detailed evaluation and analysis of both the substrates as well as the organic coatings qualities, we used the optimized conditions to investigate the limit of detection (LOD) of PAH molecules on C6ArDT/NPGD substrates. **Figure 6** shows the SERS spectra of PY, ANT, and BaP as a function of their concentration. Note that PY is detectable at 10  $\mu\text{M}$  concentration as evident by the peaks at 406, 590, 1240, and 1406  $\text{cm}^{-1}$ . On the other hand, ANT is detectable at 50  $\mu\text{M}$  concentration. While these PAH concentrations are higher than those obtained from other colloidal systems, such concentrations, which correspond to 2 and 9  $\mu\text{g/mL}$  for PY and ANT respectively, are comparable and even lower than those been observed on other surface-bound plasmonic substrates. Furthermore, the anomalies between ANT and PY might be due to difference in solubility of the molecules in the methanol, as well as the greater vdW interactions between the PY and the C6ArDT SAMs compared to those of ANT and the organic monolayers. Both of these effects are evident in the SERS results of BaP, a larger molecule with lower solubility in methanol compared to the PY and ANT. **Figure 6** also shows SERS data for BaP detected on C6ArDT/NPGDs, as well as Raman spectra of solid BaP. Note that all Raman peaks corresponding to BaP are clearly detected in the SERS spectrum of 500  $\mu\text{M}$  concentration. Furthermore, analysis of SERS spectra obtained from several BaP with descending concentrations in methanol solutions shows BaP is detected down to 6  $\mu\text{M}$  concentrations.

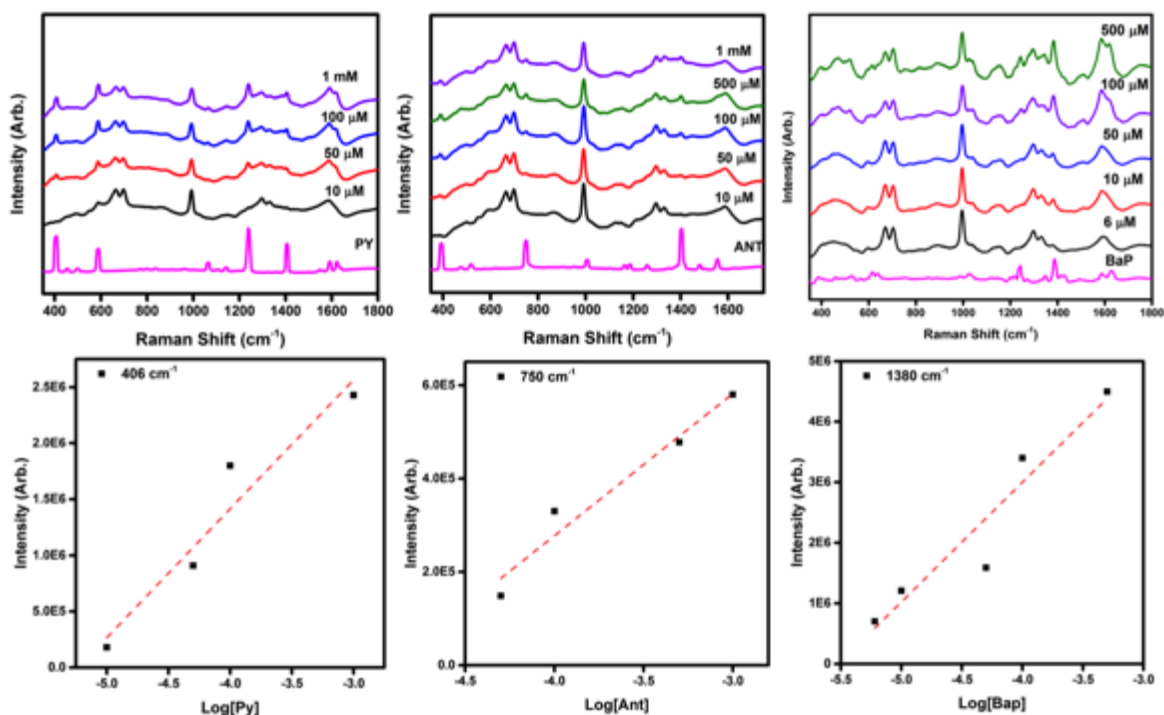


**Figure 6.** SERS spectra of Py, ANT, and Bap deposited on C6ArDT / NPGD substrates. The PAH concentration was varied to determine their lowest detectable concentration on these nanoporous substrates.

### LSPR-based sensing for PAH on NPGD

NPGD has tunable plasmon resonance that is dependent on the diameter. In our previous work, we have shown that 500 nm diameter NPGD has plasmon resonance in the near infrared (NIR) wavelength  $\sim 1200$  nm. By monitoring the resonance shift due to hydrocarbon adsorption, a sensing mechanism can be established based on LSPR extinction spectroscopy.

### Physical and optical characterization of NPGDs

First, we describe the physical nanostructural features of the NPGD substrate. The NPG disks (diameters: 350 and 600 nm) were fabricated according to methods recently published. The SEM images show the surface morphology and monolayer distribution of the patterned NPGDs on the glass coverslip (**Figures 7A-B**). With a monolayer coverage of  $\sim 50\%$ , the NPGD nanoparticles are separated in between by the bare glass surface.

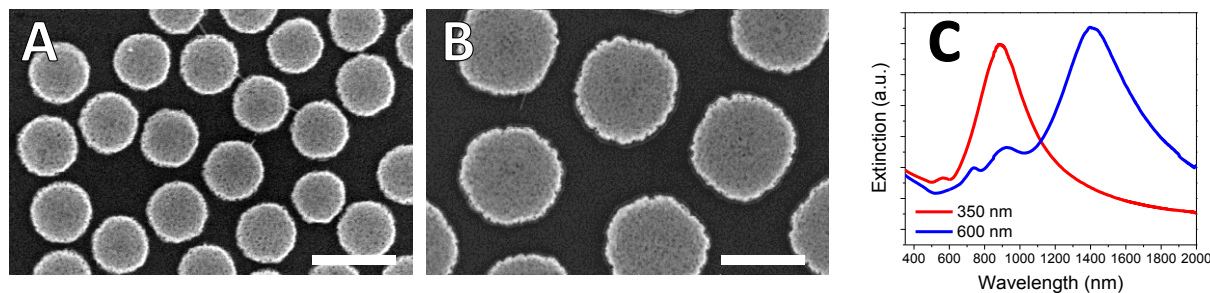


**Figure 7.** (A & B) Scanning electron microscopy (SEM) images and (C) normal-incidence far-field extinction spectra of nanoporous gold disks (NPGDs) arrays on glass in air with diameters: (A) 350 and (B) 600 nm, respectively. Scale bar is 500 nm.

The far-field extinction spectra provide information for the wavelength range where the in-plane near-field resonance, specifically unique to patterned NPG disks, is maximized. As the nanoparticle diameter size becomes larger, the in-plane LSPR peak red shifts further toward the NIR region beyond 1000 nm (**Figure 7C**). With the 600 nm diameter NPGD, the in-plane LSPR peak at 1415 nm is further red-shifted compared to the 350 nm NPG disks at 890 nm.

### LSPR sensitivity to local refractive index variations

Here we evaluate the index sensitivity of the NPG disk substrate. The LSPR peak shifts of NPG disks due to the change in refractive index in the surrounding media have been demonstrated previously. Herein, the index sensitivity of the LSPR shift of 350 nm NPG disk is evaluated by the use of various liquid samples of known refractive indices. The organic thin films, estimated to be  $\sim 10 \mu\text{m}$  in thickness using a Fabry-Perot free spectral range calculation, were sandwiched between a blank glass coverslip and a NPG disk coated glass coverslip (**Figure 8A**). The NIR extinction spectra were acquired at normal incidence. In **Figure 8B**, the LSPR of NPG disks of two diameters both red-shifted when the samples were immersed in water: from 890 nm to 1070 nm for 350 nm NPG disks; from 1415 nm to 1700 nm for 600 nm disks. It is interesting to see that the O-H combination peak at 1920 nm has been more significantly enhanced by the 600 nm disks compared to the 350 nm disks because the LSPR of 600 nm disks aligned better with the O-H peak. In **Figure 8C**, a progressive red-shift of the in-plane LSPR is observed on 350 nm disks with respect to further increase of the sample index. The index sensitivity,  $d\lambda/dn$ , was calculated to be 525.7 nm per refractive index unit (RIU) as calculated from the plot of peak shift vs.  $n$  in different media in the inset of **Figure 8C**.

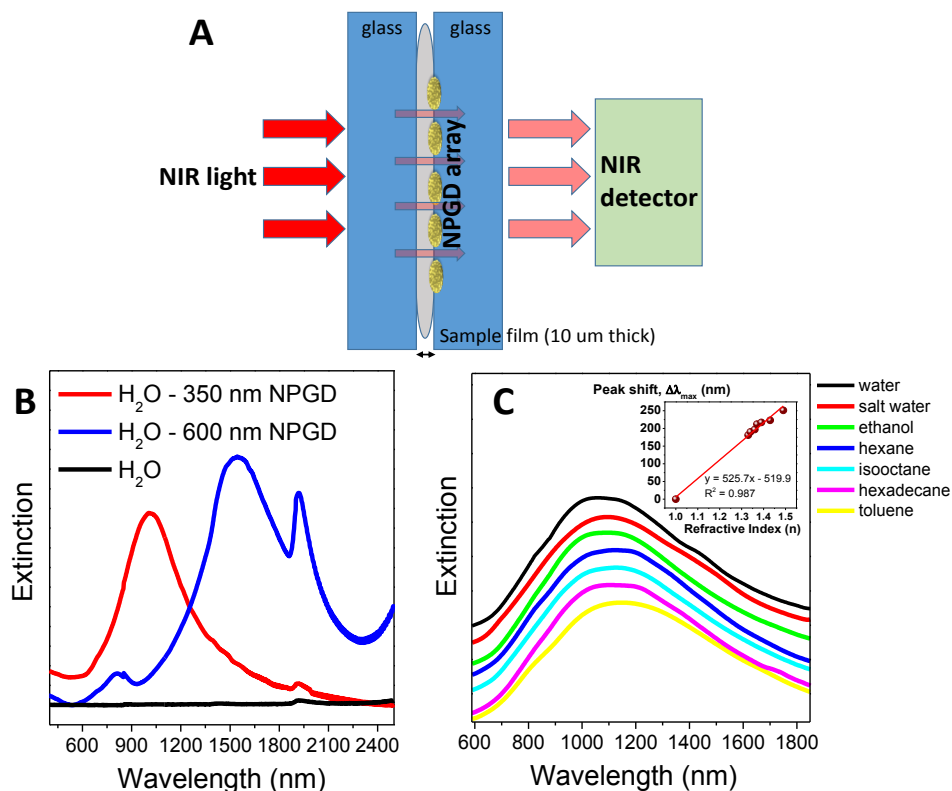


**Figure 8.** (A) Schematic diagram of the sample configuration. (B) Normal-incidence extinction spectra of water on NPG disks of two diameters: 350 and 600 nm with the O-H combination

peak at 1920 nm. (C) Normal-incidence extinction spectra of disks (350 nm diameter) in various solvents of known refractive indices varying from 1.33 to 1.49: water ( $n = 1.33$ ), 5% w/w NaCl in water ( $n = 1.34$ ), ethanol ( $n = 1.36$ ), hexane ( $n = 1.37$ ), iso-octane ( $n = 1.39$ ), hexadecane ( $n = 1.43$ ), and toluene ( $n = 1.49$ ); inset: The LSPR shift with respect to air for the corresponding refractive indices for each solvent are shown.

### Model and simulation of NPG disks

We have developed modeling techniques for NPG disk. To model the NPG disk and calculate its plasmonic properties, two different modeling approaches have been developed. A model based on the Bruggeman effective medium theory (B-EMT model) requires little information about the nanoporous structure. In contrast, the nanoporous model (NP model) retains the essential nanoporous structural features of NPG. To evaluate the performance of these models, simulated extinction spectra have been compared to the experimental data. Both the B-EMT and NP models perform well to estimate the far-field plasmon resonance peak position. However, to obtain the accurate information about the plasmon peak width/ plasmon lifetime and near field plasmonic hot-spots formation within the nanopores, the NP model is essential since the B-EMT model lacks the nanoporous network.

### B-EMT model

The B-EMT model for NPG disk can be mathematically expressed as

$$(1 - \delta_{\text{Air}}) \frac{\epsilon_{\text{Au}} - \epsilon_{\text{NPGD}}}{\epsilon_{\text{Au}} + 2\epsilon_{\text{NPGD}}} + \delta_{\text{Air}} \frac{\epsilon_{\text{Air}} - \epsilon_{\text{NPGD}}}{\epsilon_{\text{Air}} + 2\epsilon_{\text{NPGD}}} = 0 \quad (1)$$

In Eq. 1,  $\epsilon_{\text{NPGD}}$  is the effective permittivity of NPG disk,  $\epsilon_{\text{Au}}$  and  $\epsilon_{\text{Air}}$  are the permittivity of gold and air, respectively, and  $\delta_{\text{Air}}$  is the porosity or air volume fraction.  $\delta_{\text{Air}}$  can be calculated using Eq. 2 under the assumption of complete removal and preservation of silver and gold, respectively, during the de-alloying process.

$$\delta_{\text{Air}} = \frac{1 - \delta_{\text{Dealloy}} - \delta_{\text{Au}}}{1 - \delta_{\text{Dealloy}}} \quad (2)$$

$$\delta_{\text{Dealloy}} = \frac{V_{\text{Alloy Disk}} - V_{\text{NPGD}}}{V_{\text{Alloy Disk}}} \quad (3)$$

In Eq. 2,  $\delta_{\text{Au}}$  is the Au volume fraction in Ag-Au alloy disk and  $\delta_{\text{Dealloy}}$  is the volume fraction reduction due to dealloying process. Due to the existence of the adhesion layer, there was no diameter shrinkage. However, the thickness was reduced from ~76 nm to ~50 nm. This gives  $\delta_{\text{Dealloy}} \approx 0.34$ , which yields  $\delta_{\text{Air}} \approx 0.54$ . The calculated  $\delta_{\text{Air}}$  is consistent with the previously reported air volume fraction which ranges from 0.3 to 0.65 for NPG films. Besides B-EMT, the Maxwell-Garnett effective medium theory (MG-EMT) can also be employed to the NPG nanostructure. For example, Jiao et al. used the MG-EMT to estimate the porosity of patterned NPG substrate. However, the MG-EMT provides good approximation as long as the inclusion volume fraction is below 30%. When the volume fractions of the constituents are comparable in a composite material, the B-EMT is preferable. The comparable volume fractions of air (0.54) and gold (0.46) in NPG disk thus justify the use of B-EMT over MG-EMT.

### Nanoporous (NP) model

The NP model is obtained by utilizing the 2D SEM images of NPG film of comparable dimensions. The modeling relies on the following assumptions: the 3D NPG structure can be

roughly classified into ligament dominating layer (Au rich layer) and pore dominating layer (air rich layer) and these two types of layers alternate. Such assumptions are important for ensuring the bi-continuous nanostructures of NPG. For the ligament dominating layer, the tube-like ligaments are extended horizontally to form 3D meshes with pores in-between the ligaments. As for the pore dominating layer, the ligaments are extended vertically and appear to be suspended in air (porous region). **Figure 9 (a-e)** show the stepwise schematic representations for generating the NP model of NPG disk. SEM images are binarized into Au rich and air rich images via different threshold values as shown in **Figure 9a**. The binarized images are stacked into 3D ligaments as shown in **Figure 9b**. For the ligament dominating layer, nearby images are generated by gradual increase in the pore area (black part), while for pore dominating layer, same images are stacked without modification.

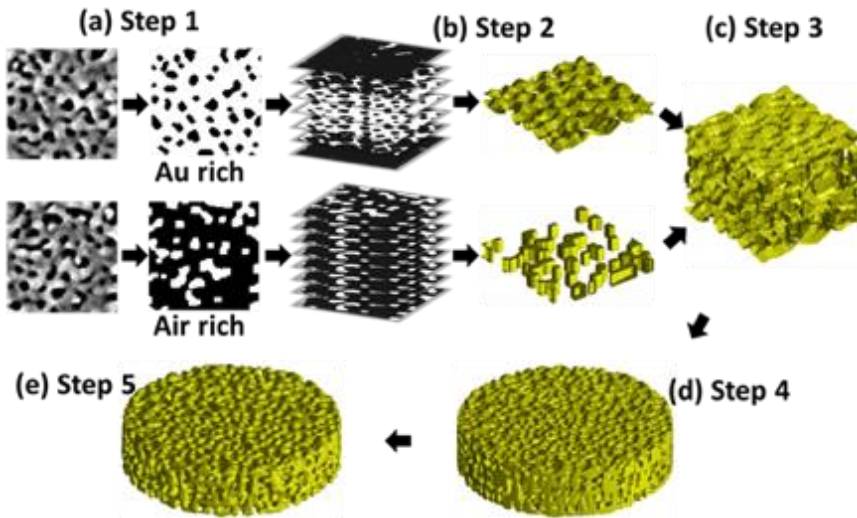


**Figure 9.** NP model of NPG disk: (a) step 1-binarization of 2D SEM images, (b) step 2-stacking of binarized images, (c) step 3-stacking of layers into NPG film, (d) step 4-disk cutting, (e) step 5-surface smoothing of as generated NPG disk.

These layers are then alternated and stacked into a thicker NPG film as shown in **Figure 9c**. During stacking, the layers are intentionally overlapped (roughly 20%) to ensure the pore-ligament continuity. In our study, 75 nm thick NPG film is generated with 5 ligament dominating and 4 pore dominating layers. Then NPG disks with desired diameter and thickness are cut out from this film as shown in **Figure 9d**. The generated NPG disk model has many sharp edges which are rounded by surface smoothing as shown in **Figure 9e**. The NP model of NPG disk has porosity ( $\delta_{Air}$ ) in the range of 52%-54%.

## Constructing instrument prototype for Ohmsett testing

### LSPR approach

The setup and the schematic drawing of the underwater LSPR sensing system are shown in **Figure 10**. The output from a whitelight lamp is coupled into the input fiber (blue) through a fiber collimator. The input fiber terminates at the underwater probe pointing at the plasmonic sample. The plasmonic sample is fixed onto an exchangeable sample plate. After passing through the plasmonic sample, the light is collected by a fiber collimator and coupled into the output

fiber (orange). The output fiber is connected to a portable spectrometer. The data are read out with a computer and the extinction spectra are calculated.

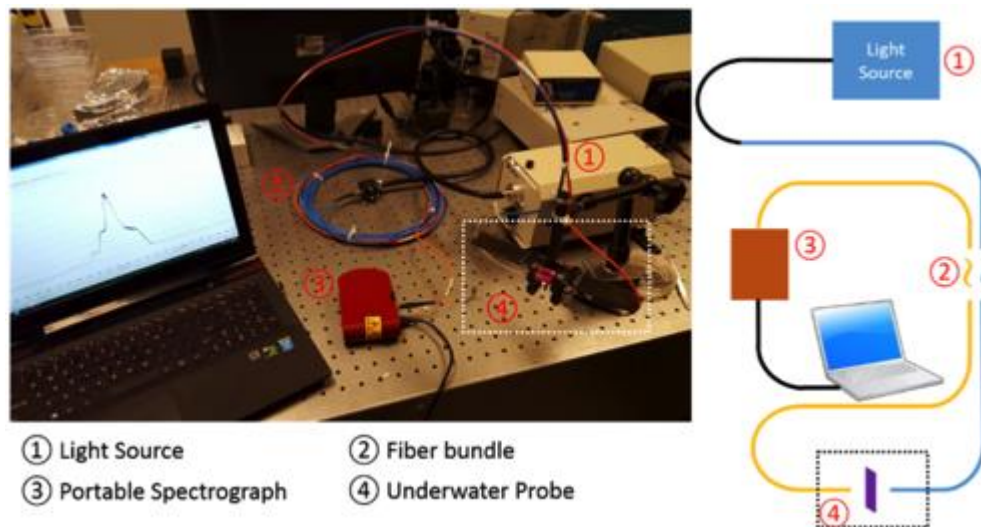


**Figure 10.** Setup of the LSPR sensing system.

### SERS approach

The setup and the schematic drawing of the underwater SERS system are shown in **Figure 11**. The laser light (785 nm) is coupled into the input fiber. The laser is focused onto the SERS substrate by the portable Raman probe. The SERS signal is also collected by the probe and coupled into the output fiber. The output fiber is connected with a spectrograph and a CCD camera. By monitoring the intensity change of the SERS signal, one can determine the analyte concentration at the SERS substrate surface. The underwater probe is consisted of a portable Raman probe fixed into a plastic case. The SERS signal is collected through a fused silica window fixed onto the plastic case. The SERS substrate is fixed onto an exchangeable sample plate that is attached to the case.

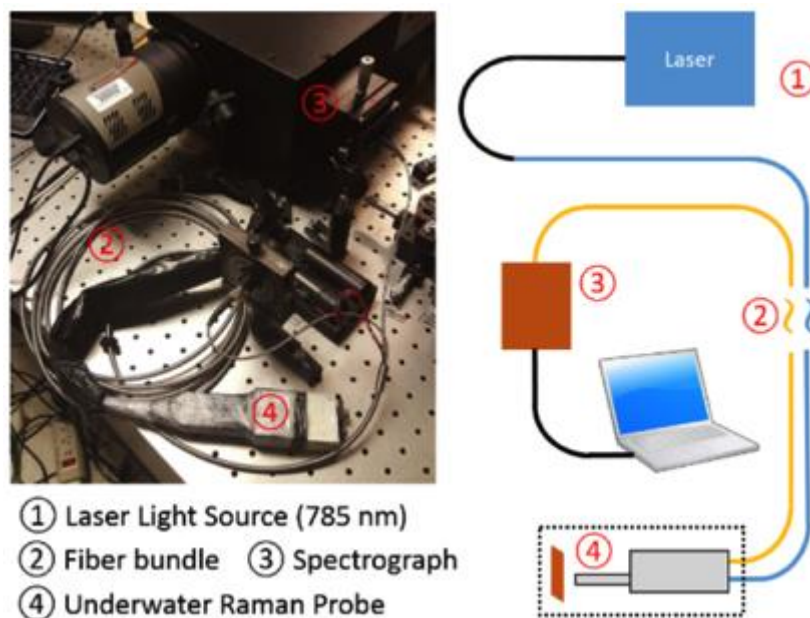


**Figure 11.** Setup and schematic of the SERS system.

## Ohmsett testing

### Background

We tested our prototypes at Ohmsett facility to obtain data using several crude oil varieties dispensed in various concentrations in test tanks. The tests were conducted during the period of November 6<sup>th</sup> – 10<sup>th</sup>, 2017. The experimental processes and results are summarized in **Table 2** and **Table 3**. Two types of experiments were conducted for sensing 4 types of crude oils and toluene. The concentrations varied within 0-9 ppm in terms of the crude oil or toluene. The PAH concentrations were therefore expected to be much lower. Crude oil samples were later submitted for laboratory PAH analysis and the results suggested PAH levels were indeed very low (sub-ppb).

**Table 2.** Crude oil tests

Injection	Stock solution	Crude oil	Toluene	Methanol	Crude oil concentration
1	10 ml	0.2 ml	4.9 ml	4.9 ml	1.1 ppm
2	10 ml	0.2 ml	4.9 ml	4.9 ml	2.3 ppm
3	10 ml	0.2 ml	4.9 ml	4.9 ml	3.4 ppm
4	10 ml	0.2 ml	4.9 ml	4.9 ml	4.6 ppm
5	10 ml	0.2 ml	4.9 ml	4.9 ml	5.7 ppm
6	10 ml	0.2 ml	4.9 ml	4.9 ml	6.9 ppm
7	10 ml	0.2 ml	4.9 ml	4.9 ml	8.0 ppm
8	10 ml	0.2 ml	4.9 ml	4.9 ml	9.1 ppm

**Table 3.** Toluene test

Injection	Toluene volume	Toluene con.
1	2 ml	10 ppm
2	8 ml	60 ppm
3	10 ml	130 ppm
4	10 ml	200 ppm
5	10 ml	260 ppm
6	10 ml	330 ppm

### LSPR sensing results

To produce a LSPR peak in the visible wavelength range, gold/silver alloy nanodisk array were employed as the sensing surface. The extinction spectra of the LSPR sensor were acquired and calculated after each step of injection. There are two modes of peak shift exist with LSPR sensing. The first one is a gradual and minor red shift (1-2 nm) in the LSPR peak position with increasing crude oil concentration and immersion time. Such shift could be induced by the dissolved crude oil being captured by the SAM. In this case, the change at the sensor surface is gradual and minor. The second LSPR shift mode is a sudden and major redshift up to few tens of nanometers. We believe such shift is caused by the non-dissolved crude oil droplet falling onto the sensor surface. In this case, the change at the surface is sudden and major. The crude oil droplet falling event happens more often at higher crude oil concentration, possibly because there

are more droplets of non-dissolved oil. Even though the droplet falling onto the sample surface will block the surface and results in sensor failing, we do note that due to a large sensing area, single droplet falling event does not block the entire surface. Additionally, the capture of crude oil droplet can also be an indicator for oil leaking. In the future, a mesh filter may be incorporated with the sensor to prevent non-dissolve oil droplets from accessing the sensing surface. To analyze the LSPR peak shift, the raw spectra were smoothed out by smoothing spline method and the peak positions were obtained by locating the extinction maximum as shown in **Table 4**. From the data, we can obtain the sensitivity of the LSPR sensor by a linear fit. The obtained sensitivities were 1.53, 2.18, 0.63 and 1.09 nm/ppm for Alaska North Slope (ANS), BAKKEN, ENDICOTT and OSEBURG respectively. The different sensitivities obtained with various crude oil samples are presumably caused by the differences in their solubility and composition.

**Table 4.** LSPR sensing results

Bakken		ANS		Endicott		Osburg	
ppm	Peak shift (nm)	ppm	Peak shift	ppm	Peak shift	ppm	Peak shift
0	0	0	0	0	0	0	0
1.1	2.4	1.1	2.1	1.1	0.6	1.1	2.3
2.3	5.5	2.3	4.2	2.3	1.7	2.3	3.1
3.4	7.1	3.4	6	3.4	2.6	3.4	3.7
4.6	14.2	4.6	7.1	4.6	2.9	4.6	5.4
5.7	28.2	5.7	48.2	5.7	3.6	5.7	7.3
6.9	29.1	6.9	50.8	6.9	53.2	6.9	8.4
8	41.4	8	60.8	8	62.6	8	9.7
9.1	49.5	9.1	62.8	9.1	N/A	9.1	10.3

### SERS Sensing results

To demonstrate the applicability of our technology, we have attached our functionalized NPGD substrates to a portable Raman sensor and performed in situ detection of toluene as well as different types of crude oil at Ohmsett facility. **Figure 12** shows the SERS spectra of toluene in water detected using our sensor. Toluene has two major Raman peaks at  $780\text{ cm}^{-1}$  and  $990\text{ cm}^{-1}$ . In addition, **Figure 12** shows that we were able to detect toluene in water at concentrations as low as 130 ppm. Note that the first Raman peak at  $780\text{ cm}^{-1}$  is clearly noticeable at the 130 ppm concentration. However, the peak at  $990\text{ cm}^{-1}$  overlaps with that of the SAM at  $1000\text{ cm}^{-1}$  as in indicated by the increase in peak broadening at  $1000\text{ cm}^{-1}$ . Analysis of peak intensity versus the concentration of toluene shows a linear dependency.

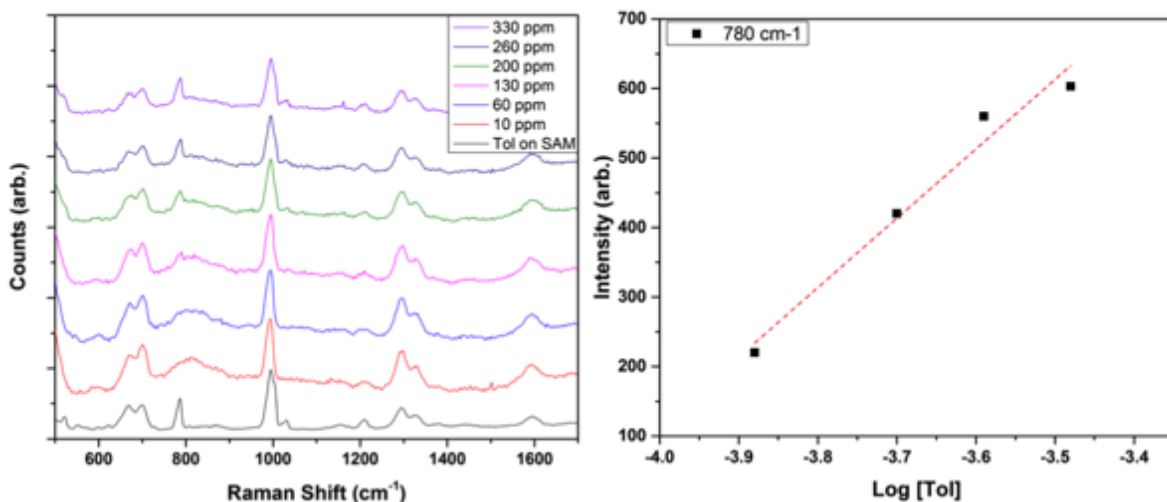


**Figure 12.** SERS spectra of in situ detection of toluene dissolved in water as well as the linear relationship of intensity versus log of toluene concentration in water.

We have also attempted to detect four different types of crude oil using our SERS sensors. Crude oil samples of Endicott, North Star, ANS, and Bakken were dissolved in methanol/toluene mixture, followed by their injection in aqueous media (**Table 2**). SERS spectra of different types of crude oil were measured and shown in **Figure 13**, from which Bakken performed the best. A clearly defined peak was detected at 419 cm<sup>-1</sup>, which might be resulting from CCC out of plane bending mode of an aromatic system. This peak was detected at oil concentration as low as 1 ppm. The gradual increase in the concentration of the crude oil results in the increase of the intensity of this peak. Other crude oil types did not show a particular Raman peak and tend to foul the sensor at concentrations as high as 8 ppm for Endicott and ANS and 6 ppm for North Star. As mentioned earlier, the PAH concentrations in the experiments (**Table 2**) were in the sub-ppb range, which were generally lower than the LOD for the SERS sensor. Nonetheless, this *in situ* SERS detection of toluene in water is a promising evidence for potential detection of water-soluble aromatic compounds.

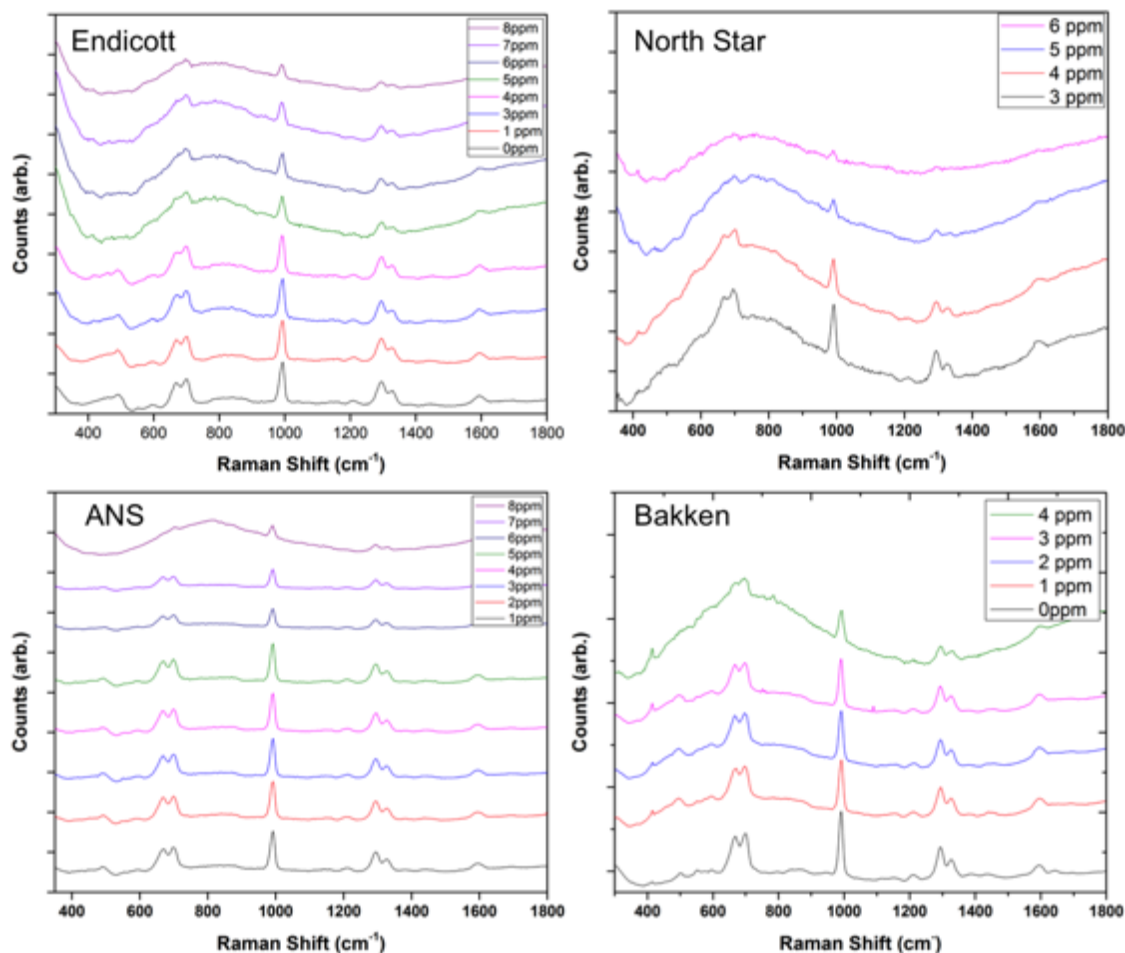


**Figure 13.** Raman spectra of crude oil detected on functionalized NPGD sensor at low concentrations (ppm range).

### Conclusion

We have developed a novel plasmonic nanostructures, nanoporous gold disks, for multi-modal spectroscopic sensing together with optical fiber technology. NPGD possess large specific surface area due to their extensive nanoporous network. NPGD also contain numerous plasmonic hot-spots throughout the porous network. For selective molecular binding of hydrocarbons, we have developed a compatible aryl-bisthiolate functional surface. Based on SERS and LSPR, we have demonstrated the detection and quantification of various polycyclic aromatic hydrocarbon species. We have developed two portable field prototype systems and tested the SERS and LSPR sensing performance at Ohmsett. The sensors were capable of detecting ppm level PAH in salt water.

### Recommendations for future work

Based on the proof of concept sensor performance, we believe further engineering can push the sensors to achieve ppm level detection of PAH and BTEX. Due to the compactness and power-efficiency of these sensors, integration with ROV and/or AUV is feasible.

## References

1. Suyan Qiu, Fusheng Zhao, Oussama Zenasni, Jingting Li, and Wei-Chuan Shih, Catalytic assembly of DNA nanostructures on nanoporous gold array as 3D architectures for label-free telomerase activity sensing, *Nanoscale Horizons* 2017
2. Suyan Qiu, Fusheng Zhao, Oussama Zenasni, Jingting Li, and Wei-Chuan Shih, Nanoporous gold disks functionalized with stabilized G-quadruplex moieties for sensing small molecules, *ACS Applied Materials & Interfaces* 2016.
3. Jingting Li, Fusheng Zhao, and Wei-Chuan Shih, Direct-write patterning of nanoporous gold microstructures by in situ laser-assisted dealloying, *Optics Express* 24(20): 23610-23617 2016.
4. Wei-Chuan Shih\*, Gregg Santos, Fusheng Zhao, Oussama Zenasni, and Masud Arnob, Simultaneous chemical and refractive index sensing in 1-2.5  $\mu\text{m}$  wavelength range on nanoporous gold disks, *Nano Letters*, 16 (7): 4641-4647 2016.
5. Gregg Santos, Felipe Ibañez de Santi Ferrara, Fusheng Zhao, Debora F. Rodrigues, and Wei-Chuan Shih, Photothermal inactivation of heat-resistant bacteria on nanoporous gold disk arrays, *Optical Materials Express* 6(4): 1217-1229 2016.
6. Jingting Li, Yong Du, Ji Qi, Ravikumar Sneha, Anthony Chang, Chandra Mohan, Wei-Chuan Shih\*, Raman spectroscopy as a diagnostic tool for monitoring acute nephritis, *Journal of Biophotonics* 9(3): 260-269 2015.
7. Ming Li, Yong Du, Fusheng Zhao, Jianbo Zeng, Chandra Mohan, and Wei-Chuan Shih\*, Reagent- and separation-free measurements of urine creatinine concentration by stamping surface-enhanced Raman scattering (S-SERS), *Biomedical Optics Express* 6(3): 849-858 2015.
8. Gregg Santos, Fusheng Zhao, Jianbo Zeng, Ming Li, and Wei-Chuan Shih\*, Zepto-mole cancer marker detection by surface-enhanced fluorescence on nanoporous gold disk substrates, *Journal of Biophotonics* 8(10): 855-863 2015.
9. Fusheng Zhao, Jianbo Zeng, and Wei-Chuan Shih\*, In situ patterning of hierarchical nanoporous gold structures by in-plane dealloying, *Materials Science and Engineering B* 194:34-40, 2015.
10. Jianbo Zeng, Fusheng Zhao, Ming Li, Chien-Hung Li, T. Randall Lee, and Wei-Chuan Shih\*, Morphological control and plasmonic tuning of nanoporous gold nanoparticles by surface modifications, *Journal of Materials Chemistry C* 3:247-252, 2015.
11. Md Masud Parvez Arnob, Fusheng Zhao, Jianbo Zeng, and Wei-Chuan Shih\*, Laser rapid thermal annealing enables tunable plasmonics in nanoporous gold nanoparticles, *Nanoscale* 6(21), 12470-12475, 2014.
12. Jianbo Zeng, Ji Qi, Fuquan Bai, Jorn Yu, and Wei-Chuan Shih\*, Analysis of ethyl and methyl centralite vibrational spectra for mapping organic gunshot residue, *Analyst* 139(17), 4270-4278, 2014.
13. Jianbo Zeng, Fusheng Zhao, Chien-Hung Li, Yifei Li, Yan Yao, T. Randall Lee, and Wei-Chuan Shih\*, Internal and external morphology-dependent plasmonic properties in nanoporous gold disks, *RSC Advances* 4, 36682-36688, 2014.
14. Ming Li, Fusheng Zhao, Jianbo Zeng, Ji Qi, Jing Lu, and Wei-Chuan Shih\*, Microfluidic surface-enhanced Raman scattering (SERS) sensor with monolithically integrated nanoporous gold disk (NPGD) arrays for rapid and label-free biomolecular detection, *Journal of Biomedical Optics* 19(11), 111611, 2014.
15. Ji Qi, Jianbo Zeng, Fusheng Zhao, Steven Hsesheng Lin, Balakrishnan Raja, Ulrich Strych, Richard C. Willson, and Wei-Chuan Shih\*, Label-free, *in situ* SERS monitoring of individual DNA hybridization in microfluidics, *Nanoscale* 6(15), 8521-8526, 2014.
16. Fusheng Zhao, Jianbo Zeng, Md Masud Parvez Arnob, Po Sun, Ji Qi, Pratik Motwani, Mufaddal Gheewala, Chien-Hung Li, Andrew Paterson, Uli Strych, Balakrishnan Raja, Richard C. Willson, John C. Wolfe, T. Randall Lee, and Wei-Chuan Shih\*, Monolithic NPG nanoparticles with large surface area, tunable plasmonics, and high-density internal hot-spots, *Nanoscale* 6, 8199-8207, 2014.
17. Ming Li, Jing Lu, Ji Qi, Fusheng Zhao, Jianbo Zeng, Jorn Chi-Chung Yu, and Wei-Chuan Shih\*, Stamping surface-enhanced Raman spectroscopy for label-free, multiplexed, molecular sensing and imaging, *Journal of Biomedical Optics* 19(5): 050501, 2014.

18. Greggy M. Santos, Fusheng Zhao, Jianbo Zeng, and Wei-Chuan Shih\*, Characterization of nanoporous gold disks for photothermal light harvesting and light-gated molecular release, *Nanoscale* 6(11), 5718-5724, 2014.
19. Ji Qi, Pratik Motwani, Mufaddal Gheewala, Christopher Brennan, John C. Wolfe, and Wei-Chuan Shih\*, Surface-enhanced Raman spectroscopy using monolithic nanoporous gold disk substrates, *Nanoscale* 5: 4105-4109, 2013. (Journal cover)